Science Advances
AAAS

advances.sciencemag.org/cgi/content/full/6/44/eabc4941/DC1

Supplementary Materials for

Early oxidation of the martian crust triggered by impacts

Zhengbin Deng*, Frédéric Moynier, Johan Villeneuve, Ninna K. Jensen, Deze Liu, Pierre Cartigny, Takashi Mikouchi, Julien Siebert, Arnaud Agranier, Marc Chaussidon, Martin Bizzarro

*Corresponding author. Email: zhengbin.deng@sund.ku.dk

Published 30 October 2020, *Sci. Adv.* **6**, eabc4941 (2020)
DOI: 10.1126/sciadv.abc4941

The PDF file includes:

Supplementary Text
Figs. S1 to S14
References

Other Supplementary Material for this manuscript includes the following:

(available at advances.sciencemag.org/cgi/content/full/6/44/eabc4941/DC1)

Data files S1 to S5

Supplementary Text

Total FeO in melt as an oxygen fugacity indicator for magnetite-saturated mafic magma.

The NWA 7533/7034 meteorites are known to have been affected by thermal resetting, e.g., magnetite-ilmenite pairs in the igneous clasts provide an equilibrium temperature range of 587-706 °C (*8*). To determine the magmatic oxygen fugacity of these clasts, a new oxybarometer that does not require the minerals to be equilibrated at magmatic temperature is needed. In the following, we show that, for a mafic silicate melt that is saturated in magnetite, its magmatic oxygen fugacity can be directly derived from its chemical composition with an oxybarometer updated after the FeTiMM method from Arató and Audétat (*17*). Arató and Audétat (*17*) noticed that the effects of alumina saturation index on TiO_2 solubility were similar to that on magnetite solubility, making the combination of Fe and Ti partitioning between magnetite and melt an oxygen fugacity indicator for silicate melts of basaltic to rhyolitic compositions, even the slowly cooled intrusive rocks like granites (*17*):

$$\Delta FMQ = \frac{\log\left(D_{FeOtot}^{mgt/melt} / D_{TiO_2}^{mgt/melt}\right) + 0.137 \times AMCNK + 0.102}{0.288 \times AMCNK + 0.054} \quad (1)$$

where ΔFMQ is oxygen fugacity in logarithmic deviation relative to the Fayalite-Magnetite-Quartz buffer, and $D_{FeOtot}^{mgt/melt}$ and $D_{TiO_2}^{mgt/melt}$ are the partition coefficients of total FeO (FeOtot) and TiO_2 between magnetite and melt, respectively. *AMCNK* is a melt compositional parameter:

$$AMCNK = X_{Al_2O_3}^{melt} / \left(X_{CaO}^{melt} + X_{Na_2O}^{melt} + X_{K_2O}^{melt} + X_{MgO}^{melt}\right) \quad (2)$$

where X_i^j stands for the molar proportion of i in phase j.

We notice that for experimental melts with MgO ≥ 3 wt% in the dataset from Arató and Audétat (*17*), the partitioning of Ti between magnetite and melt is sensitive to the Mg and Fe contents of the melt (for experimental runs with $X_{Mg}^{melt} / \left(X_{Mg}^{melt} + X_{Fe}^{melt}\right)$ = 0.284-0.596 and SiO_2 = 47.56-57.57 wt% in the quenched melts, n = 16, R^2 = 0.917; fig. S4a):

$$D_{TiO_2}^{mgt/melt} = \left(-10.2513 \pm 0.8232\right) \times \frac{X_{Mg}^{melt}}{X_{Mg}^{melt} + X_{Fe}^{melt}} + \left(7.9212 \pm 0.3914\right) \quad (3)$$

We are also aware of the definition of $D_{FeOtot}^{mgt/melt}$:

$$D_{FeOtot}^{mgt/melt} = \frac{C_{FeOtot}^{mgt}}{C_{FeOtot}^{melt}} \quad (4)$$

where C_i^j is concentration of i in phase j. After, equation 1 can be transformed into:

$$\Delta FMQ = \frac{\log\left[\left(\frac{C_{FeOtot}^{mgt}}{C_{FeOtot}^{melt}}\right) / \left(-10.2513 \times \frac{X_{Mg}^{melt}}{X_{Mg}^{melt} + X_{Fe}^{melt}} + 7.9212\right)\right] + 0.137 \times AMCNK + 0.102}{0.288 \times AMCNK + 0.054} \quad (5)$$

Since the FeOtot contents in magnetite from mafic melts (C_{FeOtot}^{mgt}) should be 65-75 wt%, ΔFMQ in equation 5 would actually be a function of the melt chemical composition (C_{FeOtot}^{melt}, X_{Mg}^{melt}, X_{Fe}^{melt} and *AMCNK*). In other words, once the saturation in magnetite is reached, the ΔFMQ of a mafic melt can be determined from its major element composition. The effects on ΔFMQ from

the uncertainties on C_{FeOtot}^{mgt}, C_{FeOtot}^{melt}, $D_{TiO_2}^{mgt/melt}$ and *AMCNK* can be quantified with the following partial differential equations:

$$\frac{\partial \Delta FMQ}{\partial C_{FeOtot}^{mgt}} = \frac{1}{C_{FeOtot}^{mgt} \times \ln(10) \times (0.288 \times AMCNK + 0.054)} \quad (6)$$

$$\frac{\partial \Delta FMQ}{\partial C_{FeOtot}^{melt}} = \frac{-1}{C_{FeOtot}^{melt} \times \ln(10) \times (0.288 \times AMCNK + 0.054)} \quad (7)$$

$$\frac{\partial \Delta FMQ}{\partial D_{TiO_2}^{mgt/melt}} = \frac{-1}{D_{TiO_2}^{mgt/melt} \times \ln(10) \times (0.288 \times AMCNK + 0.054)} \quad (8)$$

$$\frac{\partial \Delta FMQ}{\partial AMCNK} = \frac{-0.288 \times \log_{10}\left(\frac{D_{FeOtot}^{mgt/melt}}{D_{TiO_2}^{mgt/melt}}\right) - 0.021978}{(0.288 \times AMCNK + 0.054)^2} \quad (9)$$

After error propagation, the typical uncertainty on the estimated *ΔFMQ* ranges from ± 0.3-0.6 log unit for *ΔFMQ* = +0-2 to ± 0.6-1.0 log unit for *ΔFMQ* = +2-5, with which the estimated *ΔFMQ* values are consistent with the *ΔFMQ* values derived from magnetite-ilmenite pairs or experimental *ΔFMQ* values (fig. S4b). In the compiled dataset in (*17*), two runs with high SiO_2 contents of 59.03-59.73 wt% did not follow equation 3, whereas the re-estimated $D_{TiO_2}^{mgt/melt}$ using equation 3 did return to the *ΔFMQ* values fitting with their experimental *ΔFMQ* values within ± 0.5 log unit. The application of equation 5 provided *ΔFMQ* values of +0.9 ± 0.3 and +2.4 ± 0.4 for samples HEK-14-09 (Hekla volcano, Iceland) and AGU21 (Agung volcano, Sunda Arc), respectively, which have been shown to be oxide-saturated by the Ti isotopic studies in (*10*) and (*11*). These two estimated *ΔFMQ* values agree well with those calculated for oceanic island basalts (*ΔFMQ* = +0.54 ± 0.83, SD) (*57*) and arc lavas from Sunda Arc (*ΔFMQ* = +1.7-2.7) (*58*).

Furnace melting and crystallization experiments

Based on equation 5, there can be two mechanisms leading to magnetite precipitation (in other words to lower FeOtot in melt): (i) a decrease in $X_{Mg}^{melt} / \left(X_{Mg}^{melt} + X_{Fe}^{melt}\right)$ when *ΔFMQ* is constant, or (ii) an increase in *ΔFMQ* when $X_{Mg}^{melt} / \left(X_{Mg}^{melt} + X_{Fe}^{melt}\right)$ is fixed (fig. S5). For terrestrial lavas, magnetite precipitation is triggered by mechanism (i), whereas the melts equivalent to the NWA 7533 igneous clasts seem to have been controlled by mechanism (ii). While mechanism (i) can be described by melting experiments in Toplis and Carroll (*18*), and terrestrial magma differentiation, it is necessary to examine mechanism (ii) in the lab. We carried out melting and crystallization experiments at atmospheric pressures. Oxide powders (MgO-Al_2O_3-SiO_2-TiO_2-Cr_2O_3-MnO-FeO) and carbonates ($NaCO_3$-K_2CO_3-$CaCO_3$) were weighed out to make ≈ 1 g mixture shergottite-like powder. The mixture was ground in an agate mortar to reach homogenization, and aliquots of 50 mg mass were mixed into a viscous slurry and loaded on Pt loops. Since the experiments have been carried out at high fO_2 conditions, the Fe loss due to absorption into Pt wire should be negligible. The samples were heated to 1350 °C at *ΔFMQ* = −2.9 to reach a complete melting in a furnace system as described by Sossi *et al*. (*59*), and a switch of *ΔFMQ* value from −2.9 to +2.6 or +6.5 was conducted while cooling the systems to

1100-1250 °C. Oxygen fugacity was buffered by monitoring CO-CO_2 gas mixtures, and at a given temperature, the oxygen fugacity can be estimated with an accuracy of ± 0.05 log unit. An Eurotherm® controller with a thermocouple external to the alumina muffle tube allows the temperature control to be within ± 1 °C (*59*). For the runs, the cooling rate was set to be 5 °C/h, and the system stayed at the aimed temperature (1100-1250 °C) for 6-10 h to allow sufficient crystallization, after which the melt droplets were dropped into a water tank for quenching. The samples were mounted into epoxy, and measured for major element compositions by SEM at IPGP (data file S5). The results show that oxidation at a given temperature can lower magnetite solubility in mafic melts, and causes magnetite crystallization, thus leading to lower FeOtot contents but higher Mg# values in the melts (fig. S5). Using equation 5, the melts from two runs quenching at 1250 °C and 1150 °C return to ΔFMQ values of +2.5 ± 0.8 and +2.3 ± 0.8 (fig. S4b), respectively, which fit with the experimental ΔFMQ value of +2.64 ± 0.05. The melt from a run quenching at 1100 °C and air condition provides ΔFMQ = +5.1 ± 1.0, which is lower than the supposed ΔFMQ value when equilibrating with air (~ +6.5). We suspect that equation 3 cannot be exactly extrapolated to $X_{Mg}^{melt} / \left(X_{Mg}^{melt} + X_{Fe}^{melt} \right) > 0.596$ and SiO_2 = 60.6 wt%. For instance, the $D_{TiO_2}^{mgt/melt}$ value estimated for a melt with $X_{Mg}^{melt} / \left(X_{Mg}^{melt} + X_{Fe}^{melt} \right) = 0.604$ is 1.73 ± 0.63, which is higher than the measured $D_{TiO_2}^{mgt/melt}$ value of 0.92 (fig. S4a). Nonetheless, the experiments in this study can confirm that oxidation is a viable mechanism to trigger and forward magnetite crystallization at 1100-1250 °C.

Quantifying the effects from oxidation on chemical and Ti isotopic compositions of magmas.

Upon the mechanisms described, equation 3 can be used to estimate the partition coefficients of TiO_2 between magnetite and melt ($D_{TiO_2}^{mgt/melt}$) from the silicate melt composition, and equation 5 provides a link between melt oxygen fugacity and magnetite solubility if considering that *AMCNK* is fixed to be 0.35 and magnetite is the only crystallizing phase. Based on an incremental removal of Fe-Ti oxides, we can estimate the remaining Ti fractions (f_{Ti}) in the melts experiencing a redox change from $\Delta FMQ \leq -2.5$ to ΔFMQ = +3-4 from various starting melts, e.g. the melt with i) Mg# = 45 and FeOtot = 20.5 wt% or ii) Mg# = 35 and FeOtot = 20.5 wt%. While f_{Ti} after magnetite removal can be quantified, Ti isotopic fractionation factors between different melts and magnetite (usually referred as $\Delta^{49}Ti_{melt\text{-}oxide}$, i.e., the delta difference on $^{49}Ti/^{47}Ti$ ratio between the two phases) are less constrained, whereas there have been studies showing that $\Delta^{49}Ti_{melt\text{-}oxide}$ can vary between +0.1‰ and +0.5‰, depending on temperature, melt composition and oxide composition (*10, 11, 13-15, 60*). After assigning $\Delta^{49}Ti_{melt\text{-}oxide}$ values, the $\delta^{49}Ti$ of the oxidized melt after oxidation can be calculated following Rayleigh distillation:

$$\delta^{49}Ti_{oxidized\ melt} = \delta^{49}Ti_{parent\ melt} - \Delta^{49}Ti_{melt-oxide} \times \ln\left(f_{Ti}\right) \quad (10)$$

where parent melts can be assumed to have a shergottite-like $\delta^{49}Ti$ of +0.015‰. Considering that $\Delta^{49}Ti_{melt\text{-}oxide}$ increases with lower temperature and more silicic melt composition (*10, 11, 13-15, 60*), we can reasonably assign the $\Delta^{49}Ti_{melt\text{-}oxide}$ to be +0.2‰ at Mg# = 45 and to be +0.4‰ at Mg# = 35. Afterwards, we can observe that for parent melts with lower Mg# values, oxidation can result in larger Ti isotopic fractionations in the differentiated melts (Fig. 2 and fig. S6), arising from their higher $D_{TiO_2}^{mgt/melt}$ and $\Delta^{49}Ti_{melt\text{-}oxide}$ values.

The Ni concentrations in the melt after oxidation can also be estimated with an incremental removal of Fe-Ti oxides after assigning Ni = 1750 ppm and FeOtot = 20.5 wt% to the parent melt, as well as $D_{Ni}^{mgt/melt}$. The Ni-FeOtot systematics of the NWA 7034/7533 igneous clasts can be reproduced by continuous Fe-Ti oxide removal with $D_{Ni}^{mgt/melt}$ = 13 (Fig. 3). While the δ^{49}Ti-Mg# systematics of the differentiated melts are quite sensitive to the inconsistent $D_{TiO_2}^{mgt/melt}$ and $\Delta^{49}Ti_{melt\text{-}oxide}$ values in parent melts with various Mg# values (or MgO contents), the differentiated melts should follow almost the same oxide-controlled trajectory on the Ni vs. FeOtot plot, as soon as these parent melts have been assigned to have the same FeOtot contents and Ni concentrations. This explains why the NWA 7533/7034 clasts provide a continuous Ni vs. FeOtot pattern (Fig. 3), whereas their distribution seems more scattered on the δ^{49}Ti vs. Mg# plot (Fig. 2). The effects on V and Co in melts can be also quantified following an incremental removal of Fe-Ti oxides.

Quantifying oxygen contribution in the melts from the oxidant.

After estimating the ΔFMQ values of the silicate melts, the oxygen contribution from the oxidant can be calculated. Note that 10 wt% addition of rocky material from the impactors may alter the oxygen fugacity of the melts by sub log unit, depending on the oxidation state of possible chondritic impactors. While the types of the chondritic impactor are less constrained, we temporarily consider that oxidation of melt can be represented by reaction with free oxygen coming from decomposition of water:

$$4FeO(melt) + O_2(gas) = 2Fe_2O_3(melt) \quad (11)$$

$$FeO(melt) + Fe_2O_3(melt) = Fe_3O_4(magnetite) \quad (12)$$

The ferric-ferrous ratio of silicate melt is a function of oxygen fugacity, temperature, pressure and composition as shown by Gaillard *et al*. (*61*):

$$\ln\left(\frac{X_{Fe_2O_3}^{melt}}{X_{FeO}^{melt}}\right) = 0.196\times\ln(10)\times\left[\Delta FMQ + \frac{25096 - 0.11\times(P-1)}{T} - 8.735\right] + \frac{1.1492\times10^4}{T} - 6.675 + \sum d_i X_i^{melt} \quad (13)$$

where T is temperature in K, P is pressure in bar, d_i is coefficient for i in melt, and X_i^{melt} is molar proportion of i in melt. The uncertainty on $X_{Fe_2O_3}^{melt} / X_{FeO}^{melt}$ can be estimated from the partial differential equations from equation 13:

$$\frac{\partial\left(\frac{X_{Fe_2O_3}^{melt}}{X_{FeO}^{melt}}\right)}{\partial\Delta FMQ} = 0.196\times\ln(10)\times\frac{X_{Fe_2O_3}^{melt}}{X_{FeO}^{melt}} \quad (14)$$

$$\frac{\partial\left(\frac{X_{Fe_2O_3}^{melt}}{X_{FeO}^{melt}}\right)}{\partial P} = \frac{-0.02156\times\ln(10)}{T}\times\frac{X_{Fe_2O_3}^{melt}}{X_{FeO}^{melt}} \quad (15)$$

$$\frac{\partial\left(\frac{X_{Fe_2O_3}^{melt}}{X_{FeO}^{melt}}\right)}{\partial T}=\frac{-0.196\times\ln(10)\times\left[25096-0.11\times(P-1)\right]-1.1492\times10^4}{T^2}\times\frac{X_{Fe_2O_3}^{melt}}{X_{FeO}^{melt}} \quad (16)$$

To oxidize a reduced parent melt containing negligible ferric iron (e.g., $\Delta FMQ \leq -2.5$), the oxygen contribution from the oxidant in the oxidized melt ($f_{O-oxidant}^{melt}$) can be approximated to:

$$f_{O-oxidant}^{melt}\approx\frac{X_{FeOtot}^{melt}\times\left(\frac{2\times\frac{X_{Fe_2O_3}^{melt}}{X_{FeO}^{melt}}}{2\times\frac{X_{Fe_2O_3}^{melt}}{X_{FeO}^{melt}}+1}\right)\times\frac{1}{2}+\left(X_{FeOtot}^{parent\ melt}-X_{FeOtot}^{melt}\right)\times\frac{1}{3}}{\sum\beta_i X_i^{melt}} \quad (17)$$

where β_i represents the oxygen number in oxide i with molecular formula of $x_\alpha O_\beta$. The uncertainty on $f_{O-oxidant}^{melt}$ can be estimated from the errors from $X_{Fe_2O_3}^{melt}$ / X_{FeO}^{melt} and X_{FeOtot}^{melt}:

$$\frac{\partial\left(f_{O-oxidant}^{melt}\right)}{\partial\left(\frac{X_{Fe_2O_3}^{melt}}{X_{FeO}^{melt}}\right)}=\frac{X_{FeOtot}^{melt}}{\left(2\times\frac{X_{Fe_2O_3}^{melt}}{X_{FeO}^{melt}}+1\right)^2}\times\frac{1}{\sum\beta_i X_i^{melt}} \quad (18)$$

$$\frac{\partial\left(f_{O-oxidant}^{melt}\right)}{\partial\left(X_{FeOtot}^{melt}\right)}=\left[\left(\frac{2\times\frac{X_{Fe_2O_3}^{melt}}{X_{FeO}^{melt}}}{2\times\frac{X_{Fe_2O_3}^{melt}}{X_{FeO}^{melt}}+1}\right)\times\frac{1}{2}-\frac{1}{3}\right]\times\frac{1}{\sum\beta_i X_i^{melt}} \quad (19)$$

Assuming FeOtot = 20.5 wt% for parent melt and a temperature of 1100 °C, integration of the equations above provides $f_{O-oxidant}^{melt}$ values of 0.024 ± 0.006, 0.026 ± 0.007 and 0.029 ± 0.008 for the igneous clasts C16, C7 and C27, respectively. Afterwards, the effects from impact-induced oxidation on the melt $\Delta^{17}O$ would be dependent on the oxygen contributions from the oxidant (water or perchlorates) and rocky impactor (i.e., $f_{O-oxidant}^{melt}$ and $f_{O-rocky\ impactor}^{melt}$, respectively):

$$\begin{aligned}&\Delta^{17}O_{oxidized\ melt}-\Delta^{17}O_{parent\ melt}\\&\approx\left(\Delta^{17}O_{oxidant}-\Delta^{17}O_{parent\ melt}\right)\times f_{O-oxidant}^{melt}+\left(\Delta^{17}O_{rocky\ impactor}-\Delta^{17}O_{parent\ melt}\right)\times f_{O-rocky\ impactor}^{melt}\end{aligned} \quad (20)$$

where $\Delta^{17}O_i$ is the $\Delta^{17}O$ value of i. Once $f_{O-oxidant}^{melt}$ and $f_{O-rocky\ impactor}^{melt}$ have been quantified based on oxygen fugacity change and highly siderophile element concentrations, respectively, the effects from oxidation on the $\Delta^{17}O$ values of oxidized melts would depend on the $\Delta^{17}O$ differences of oxidant and rocky impactor relative to the reduced parent melt (equation 20).

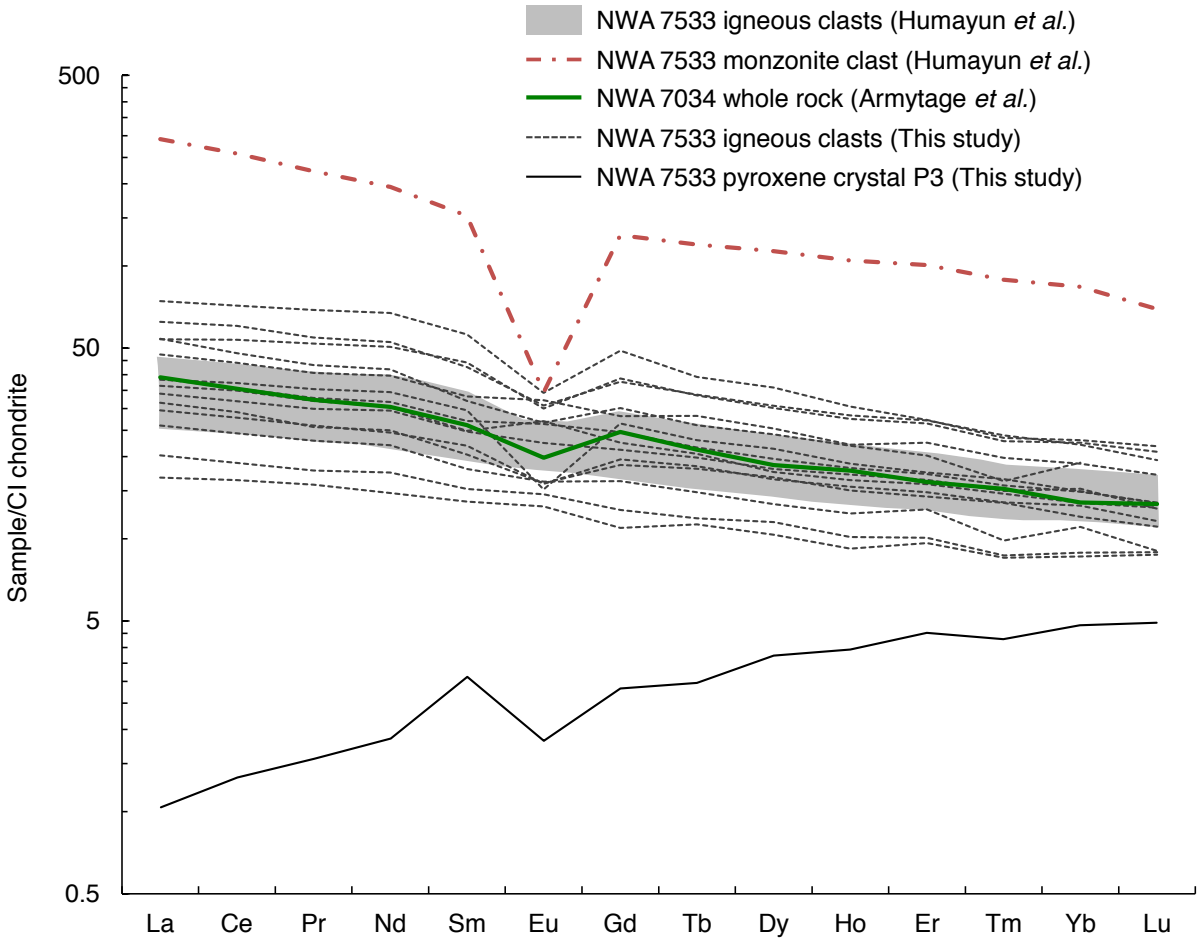

Fig. S1.

Rare earth element abundances of the NWA 7533/7034 igneous clasts after a normalization onto CI chondrite values (*39*). Data of the NWA 7533 igneous clasts with a unique monzonite clast (*3*) and whole rock NWA 7034 meteorite (*31*) are also shown.

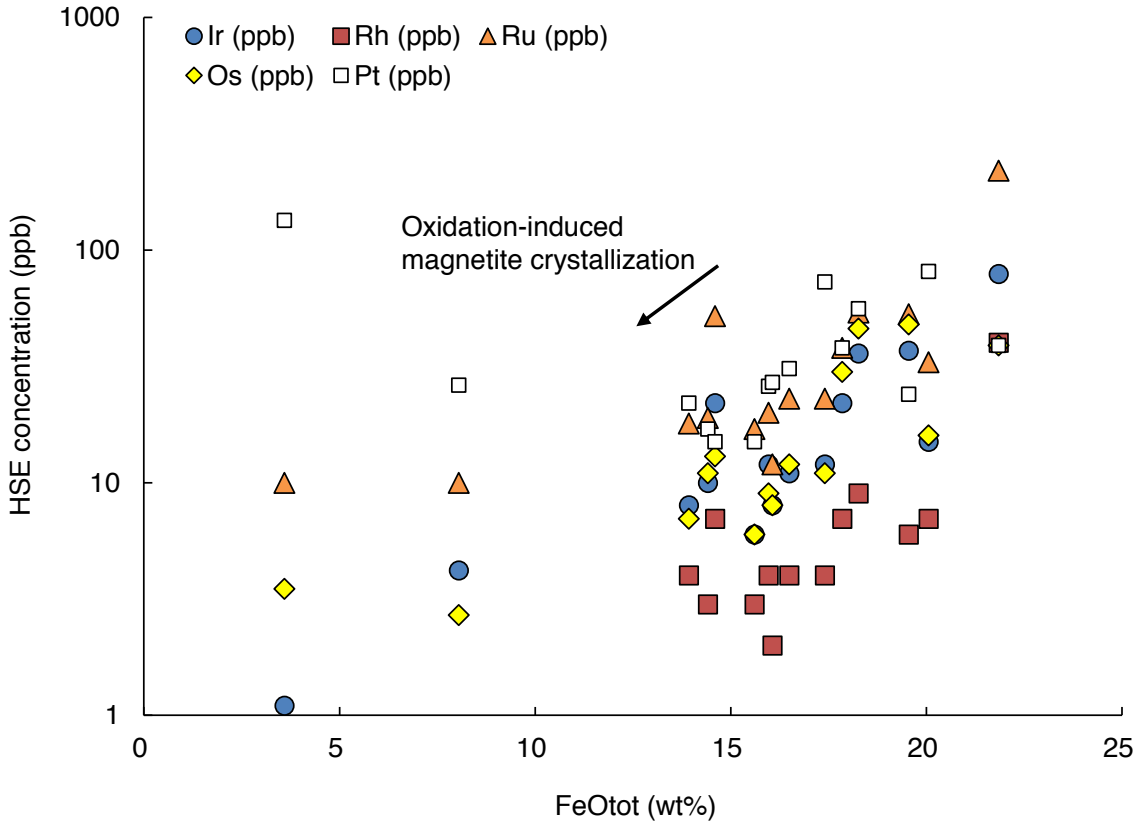

Fig. S2.

Highly siderophile element (HSE) abundances and FeOtot contents of the NWA 7533 clasts obtained by laser ablation measurements in Humayun *et al*. (*3*).

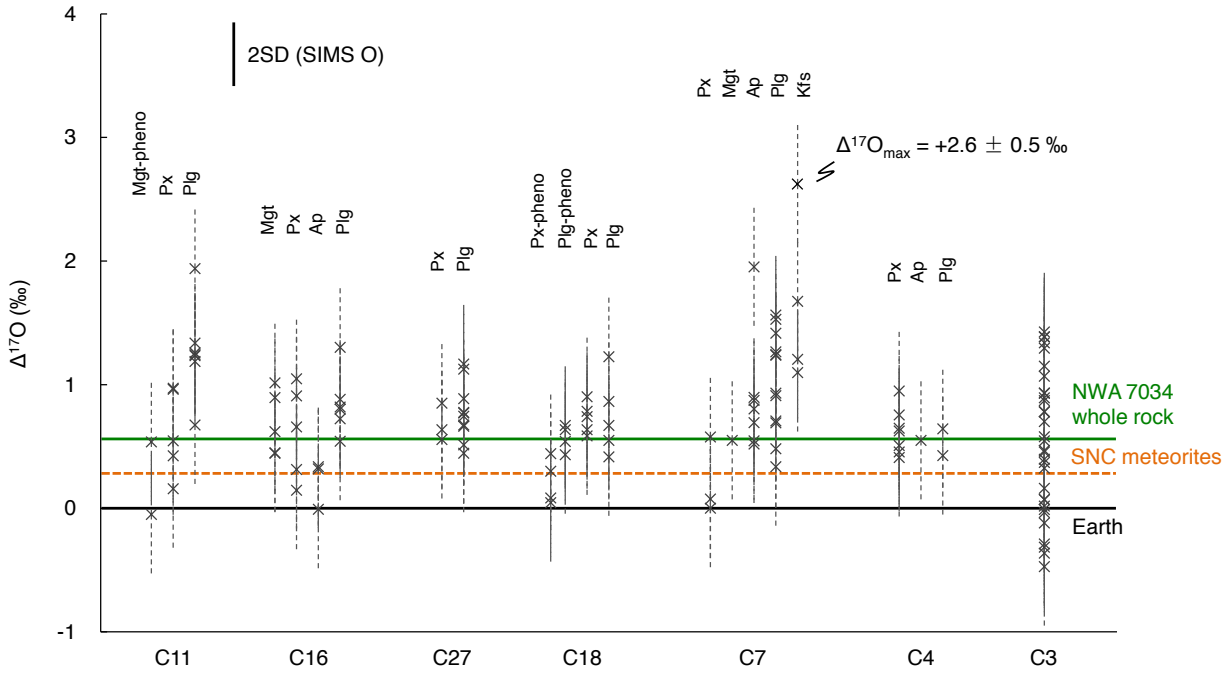

Fig. S3.

In situ triple O isotopic results on seven NWA 7533/7034 igneous clasts obtained by SIMS measurements in this study. The values for whole rock NWA 7034 meteorite (*4*), SNC meteorites (*41*) and the Earth are also shown.

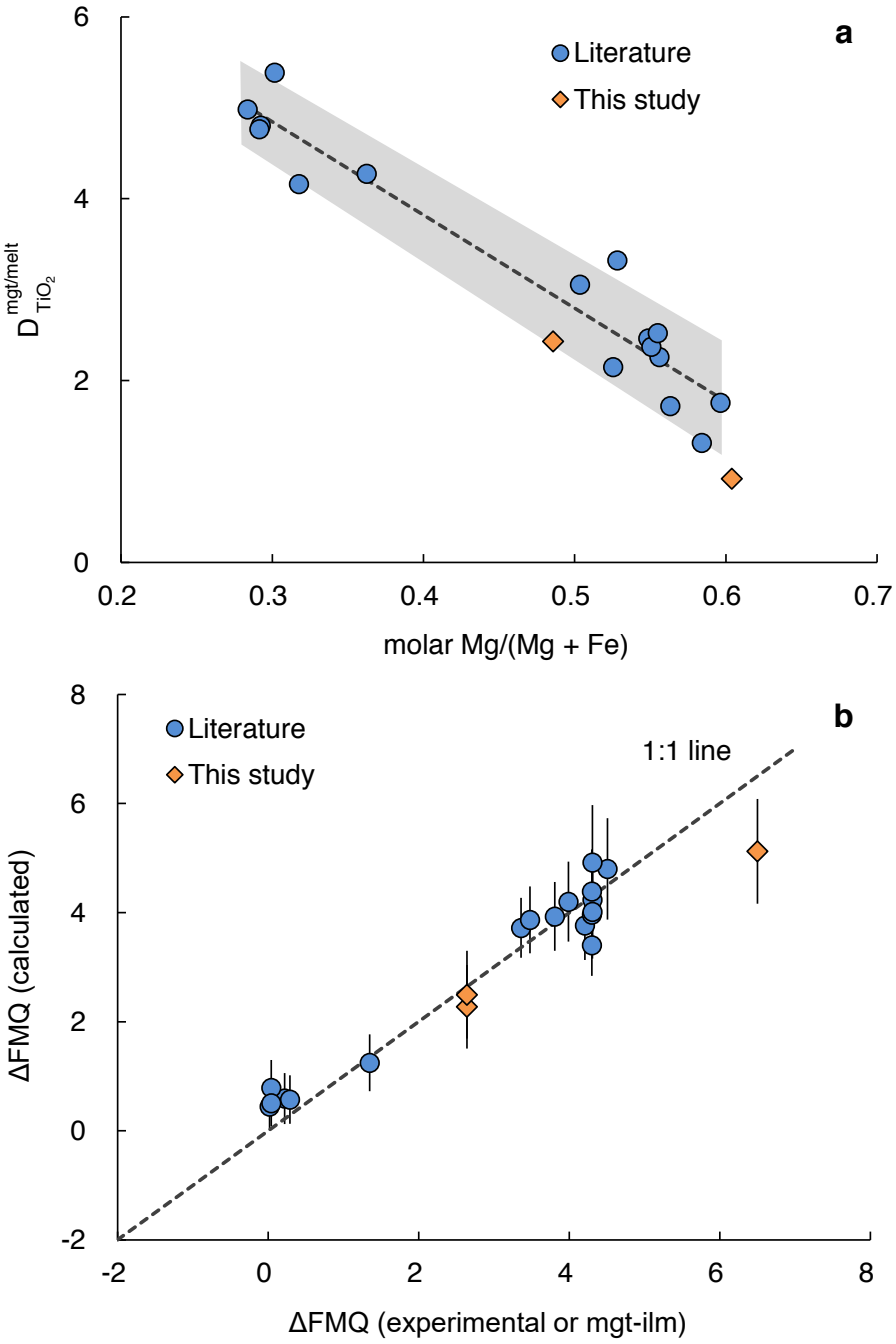

Fig. S4.

(**a**) Plot showing the correlation between $D^{mgt/melt}_{TiO_2}$ and melt Mg# in 16 experimental runs from the compilation in Arató and Audétat (*17*), except for two runs with high SiO_2 contents of 59.03-59.73 wt%. (**b**) Plot comparing the ΔFMQ values calculated from the oxybarometer updated after Arató and Audétat (*17*) with the values from experimental settings or those estimated using magnetite-ilmenite pairs (*17*). Results from the experimental runs in this study are also shown.

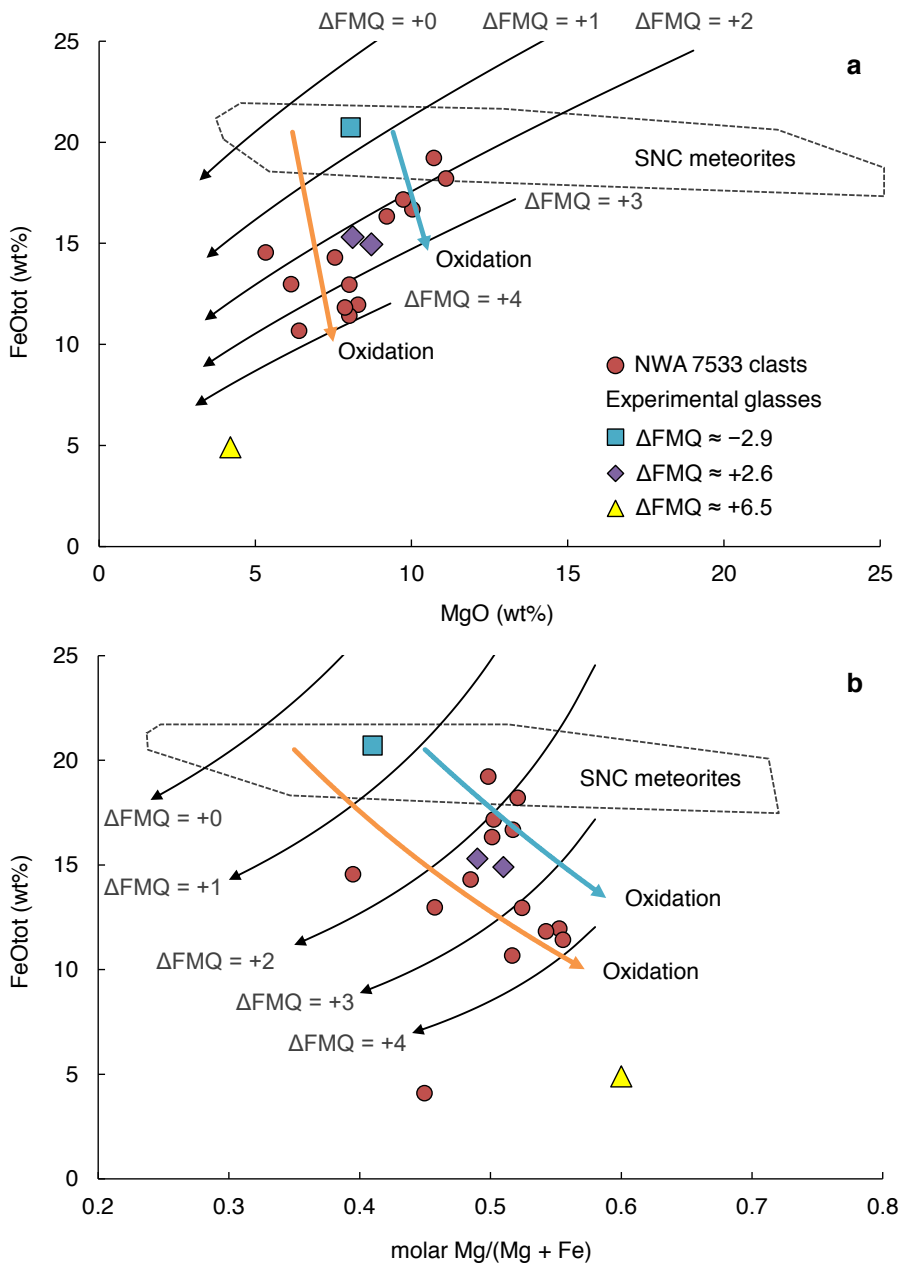

Fig. S5.

Plots of FeOtot versus MgO (**a**) and FeOtot versus molar Mg/(Mg + Fe) (**b**) for the NWA 7533 clasts and experimental glass samples at ΔFMQ values of −2.9, +2.6 and +6.5 from the furnace experiments in this study. The black curves show the compositional variations predicted by equation 5 for oxide-saturated silicate melts at ΔFMQ values of +0, +1, +2, +3 and +4, assuming the AMCNK value fixed to be 0.35. The two colored trajectories with arrow represent the effects from oxide removal, caused by oxidation of the basaltic shergottite-like melts (FeOtot = 20.5 wt%) at Mg# values of 35 (the orange) and 45 (the blue).

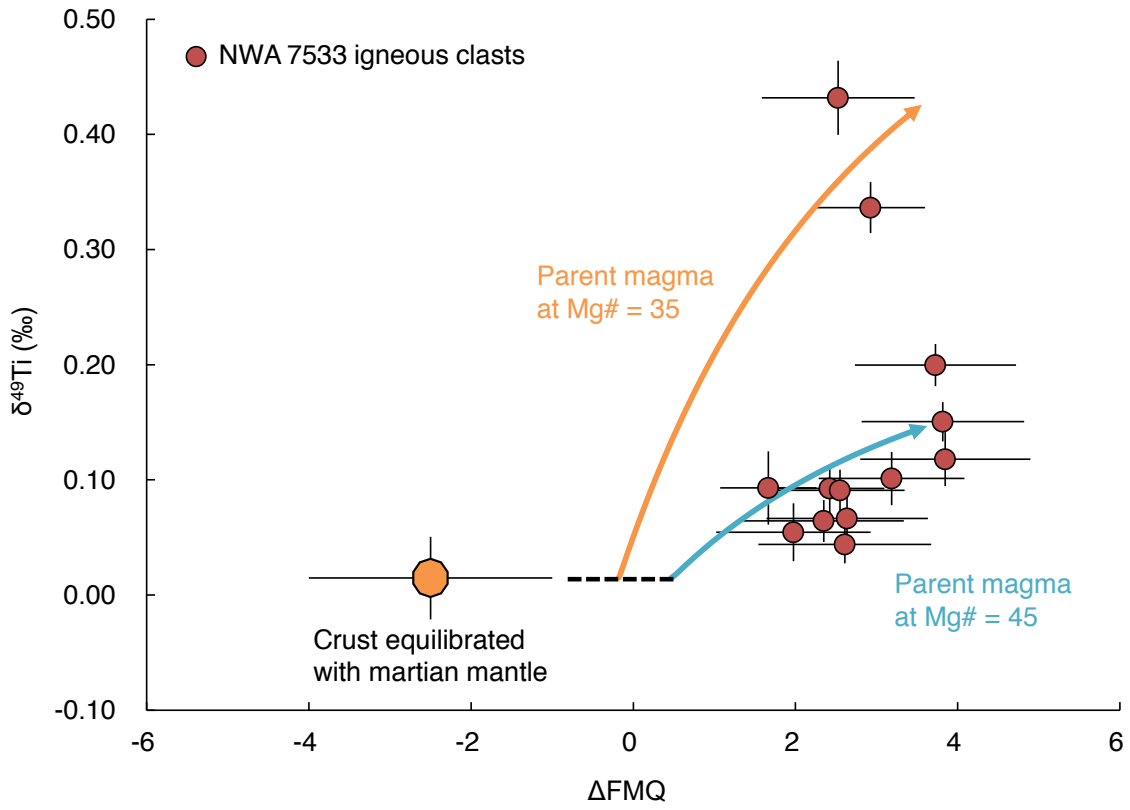

Fig. S6.

Plot of δ^{49}Ti versus ΔFMQ for the NWA 7533 clasts. The crust at equilibrium with martian mantle is considered to have a δ^{49}Ti value of +0.015 ± 0.036‰ based on the Ti isotopic results from shergottites in this study, and an average ΔFMQ value of −2.5 ± 1.5 (*6*). The two colored trajectories with arrow represent the effects from oxide removal, caused by oxidation of the basaltic shergottite-like melts (FeOtot = 20.5 wt%) at Mg# values of 35 (the orange) and 45 (the blue).

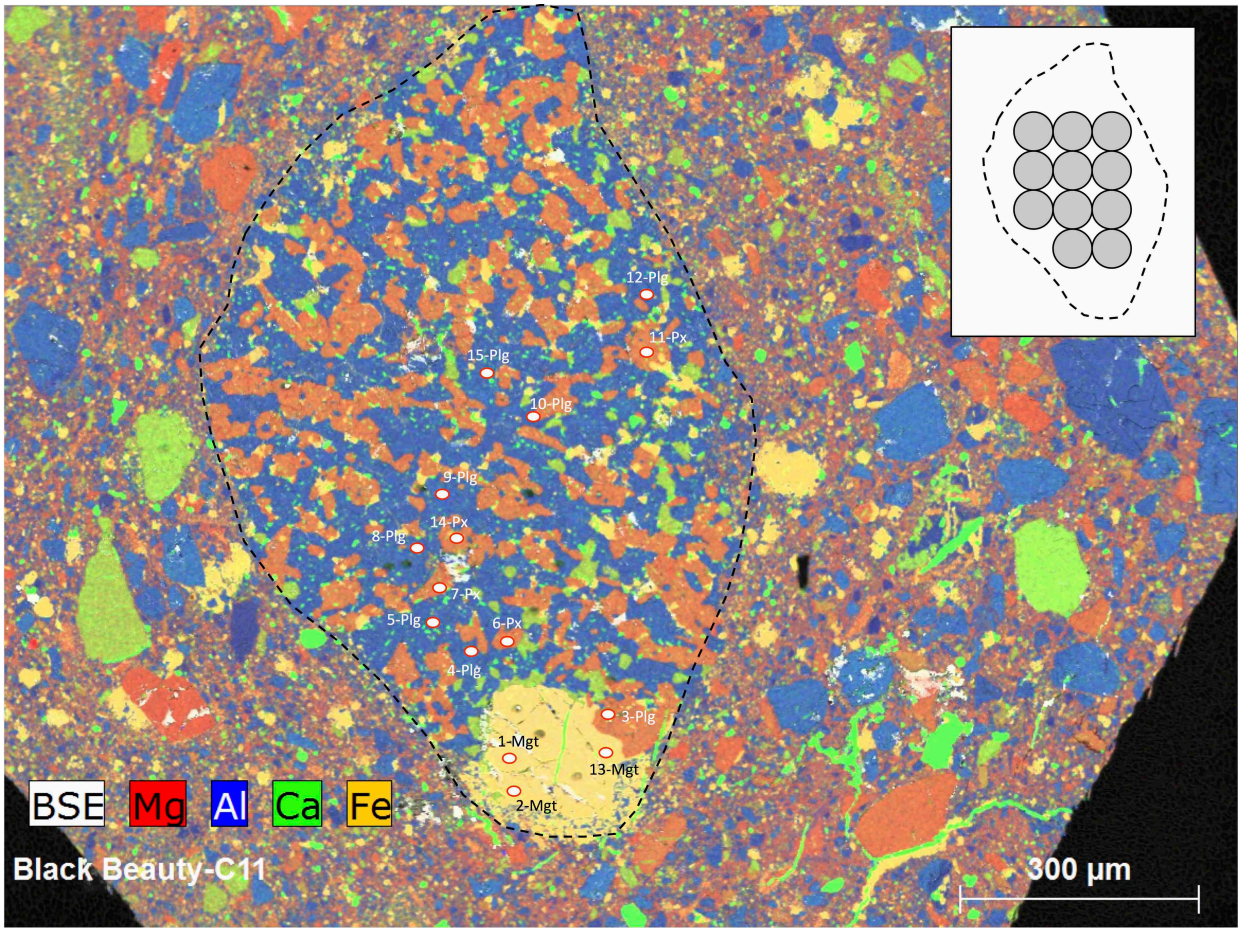

Fig. S7.

Chemical map with SIMS (~15 µm) and laser ablation (~160 µm in the inset) spots for clast C11.

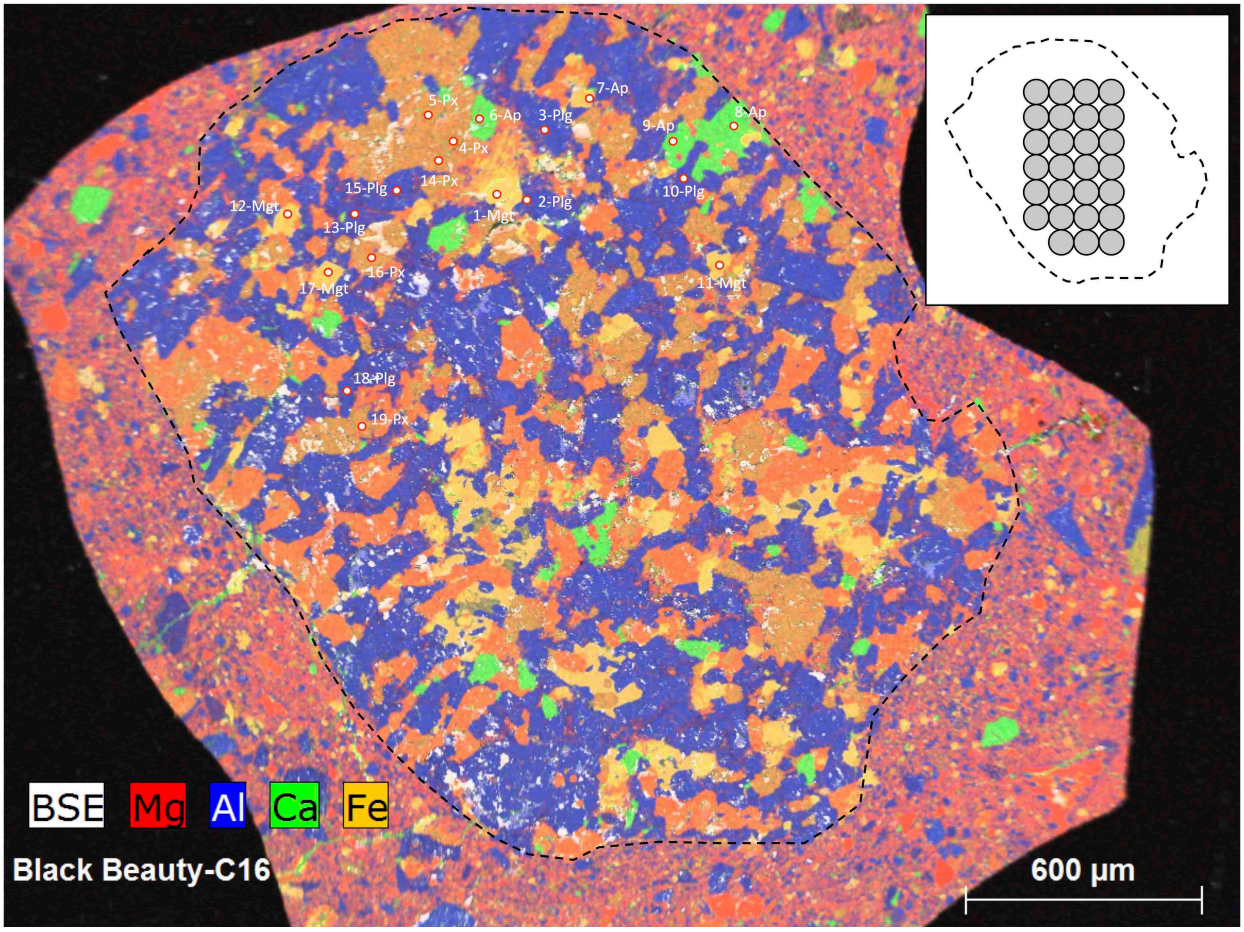

Fig. S8.
Chemical map with SIMS (~15 µm) and laser ablation (~160 µm in the inset) spots for clast C16.

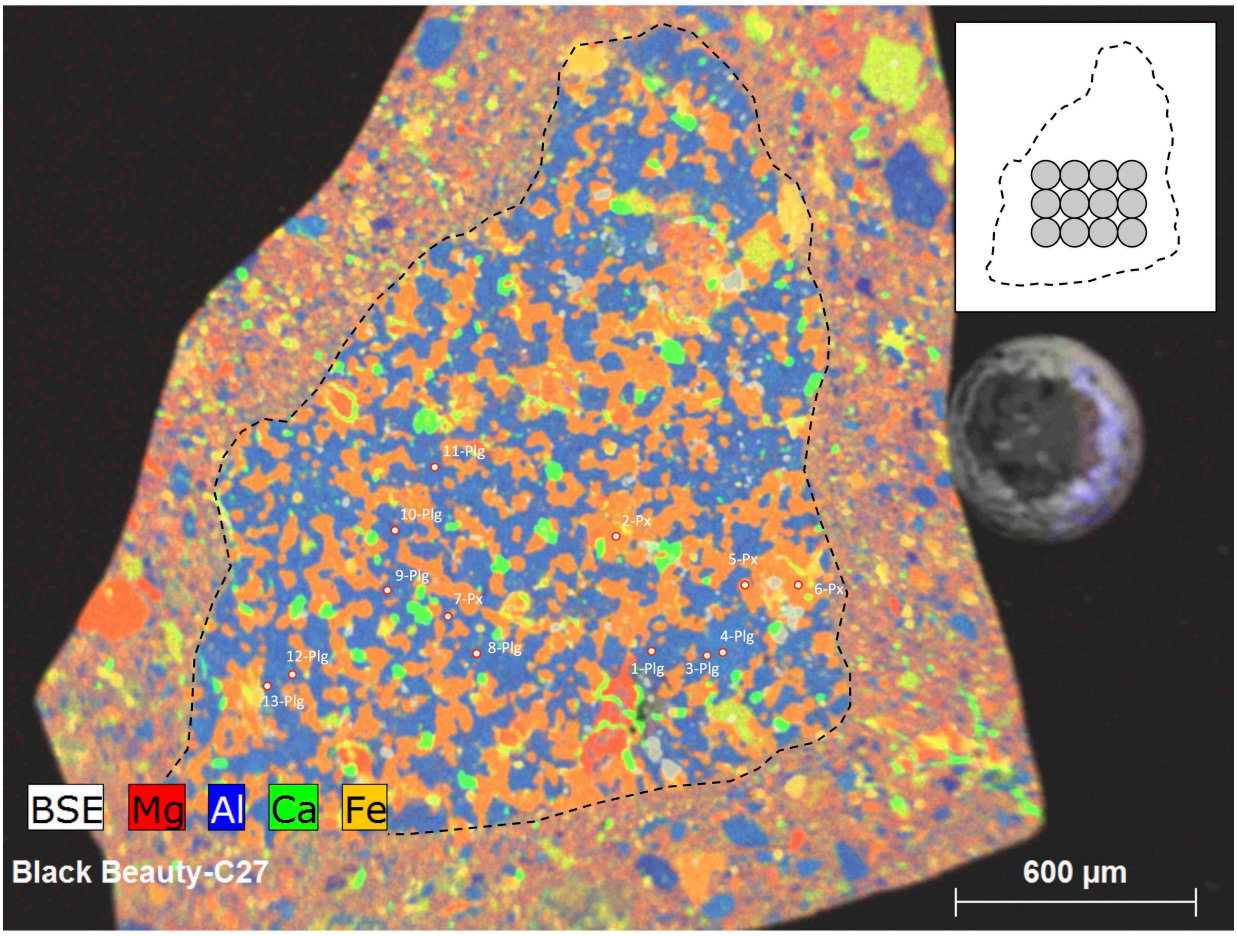

Fig. S9.

Chemical map with SIMS (~15 µm) and laser ablation (~160 µm in the inset) spots for clast C27.

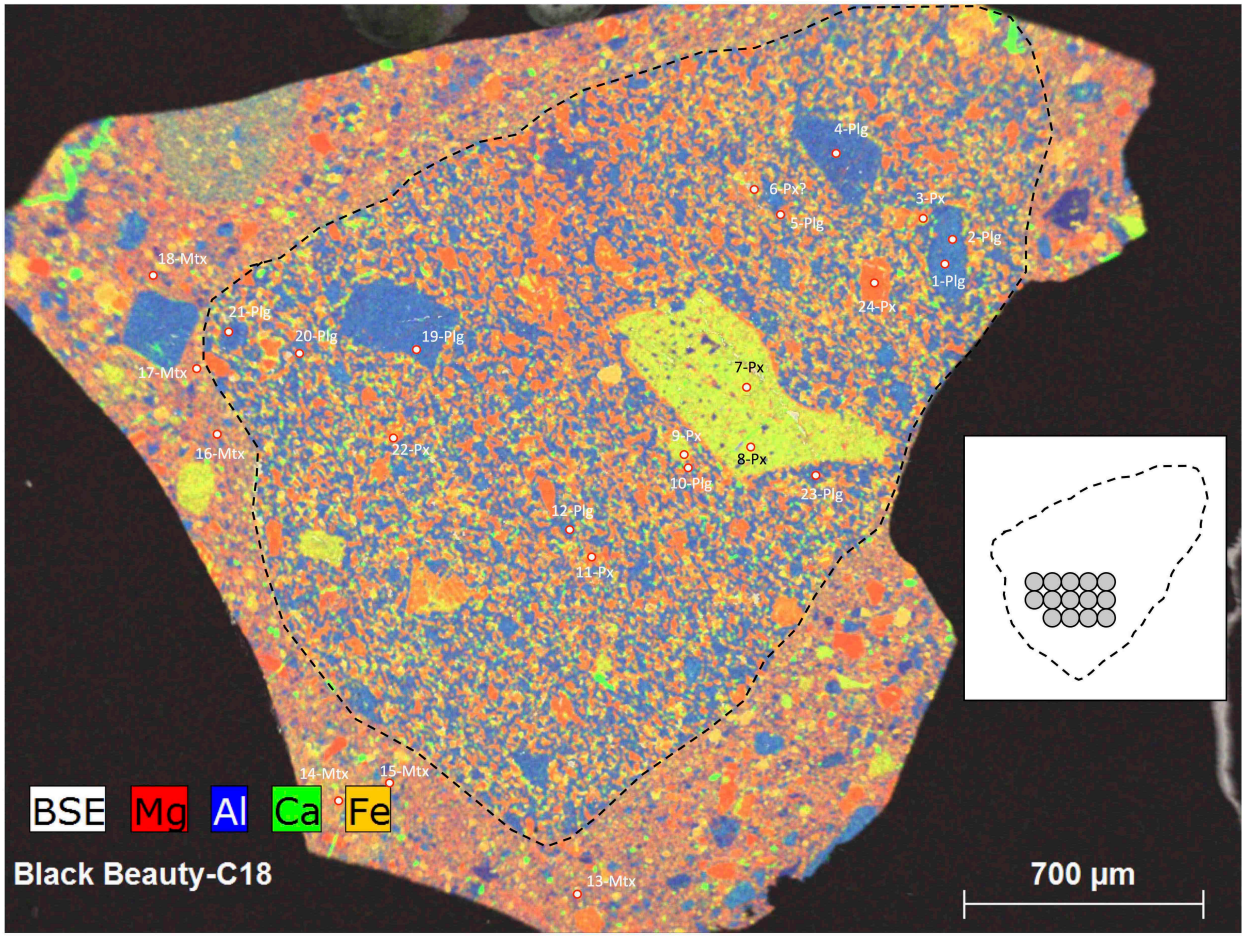

Fig. S10.

Chemical map with SIMS (~15 µm) and laser ablation (~160 µm in the inset) spots for clast C18.

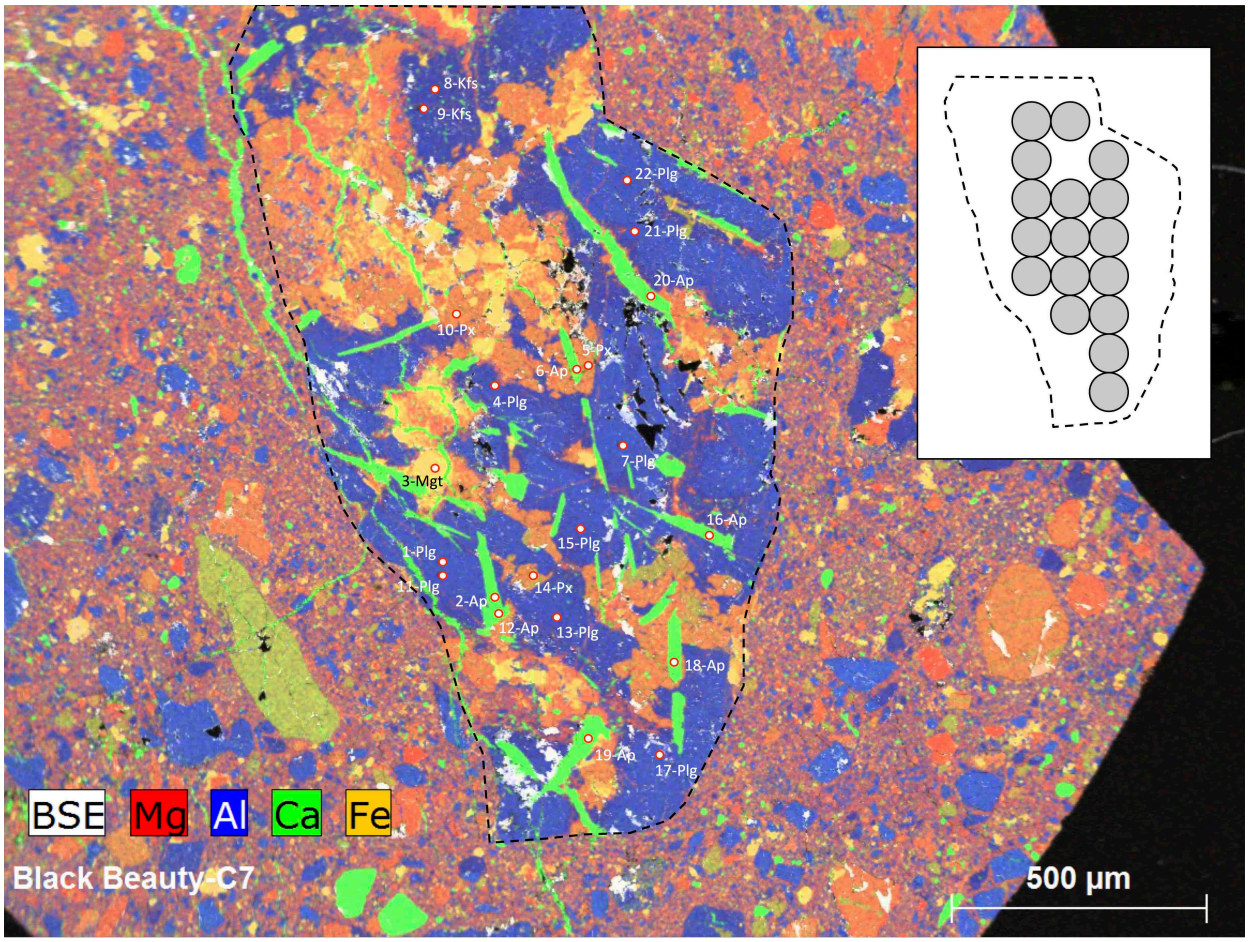

Fig. S11.

Chemical map with SIMS (~15 µm) and laser ablation (~160 µm in the inset) spots for clast C7.

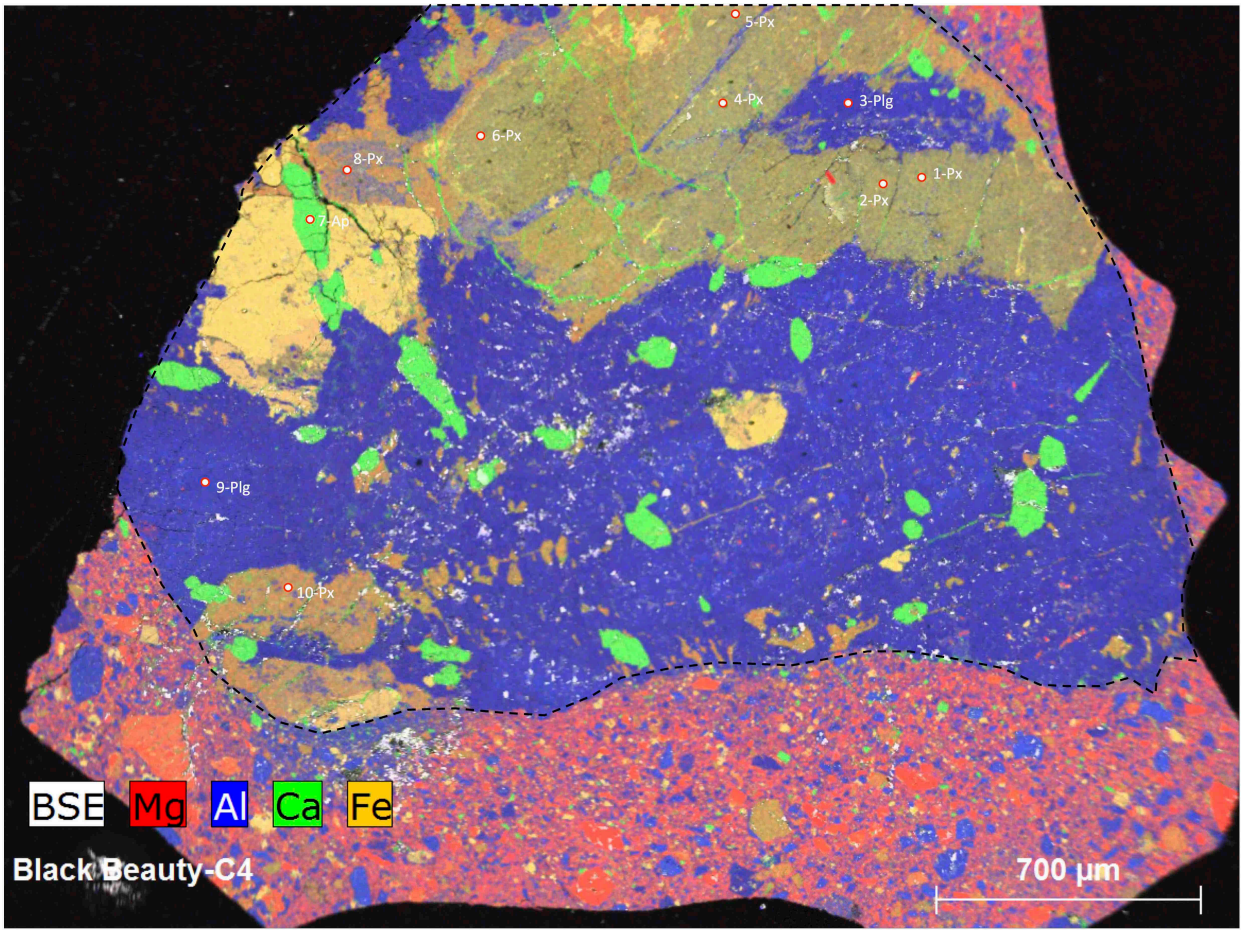

Fig. S12.
Chemical map with SIMS (~15 µm) spots for clast C4.

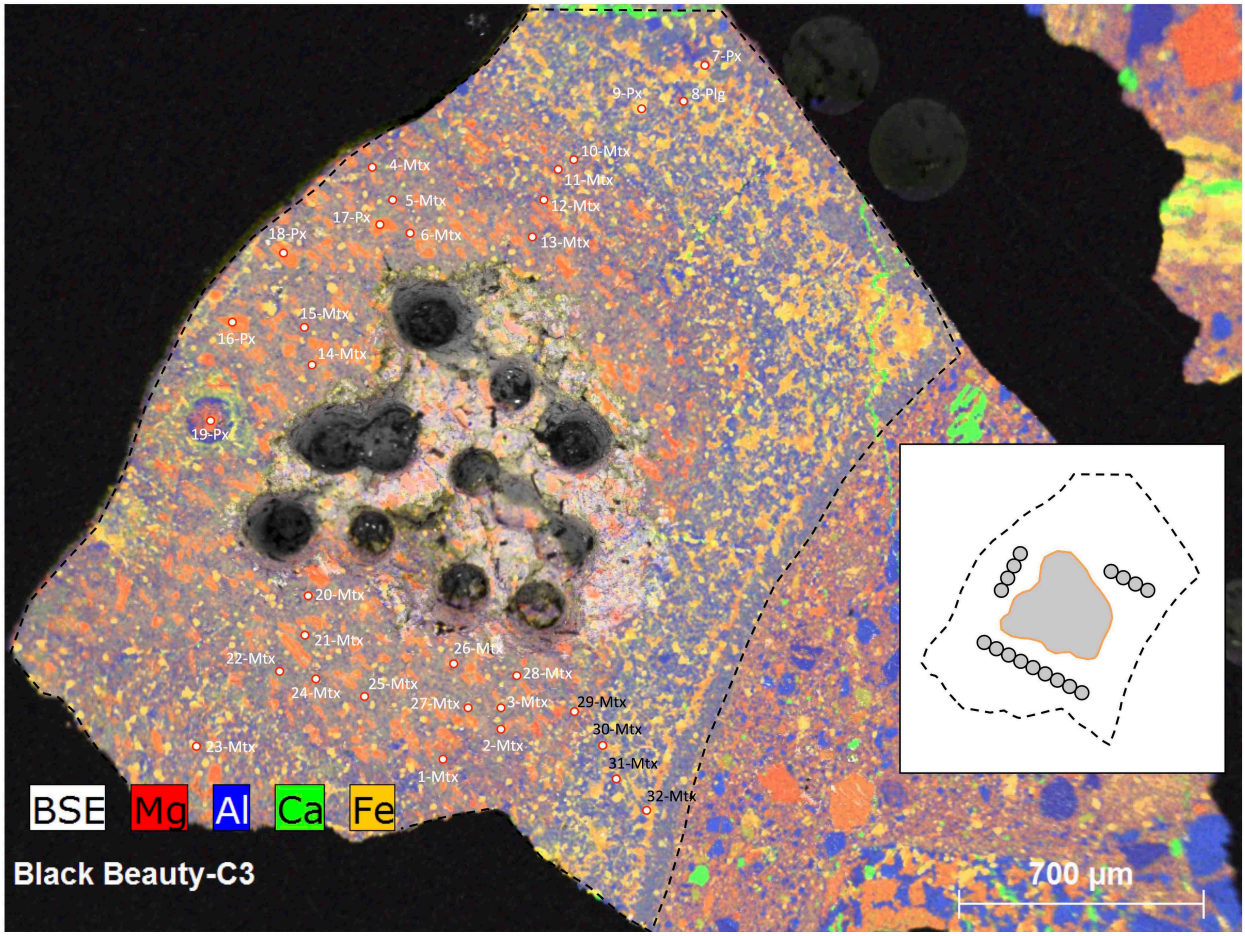

Fig. S13.
Chemical map with SIMS (~15 µm) and laser ablation (~160 µm in the inset) spots for clast C3.

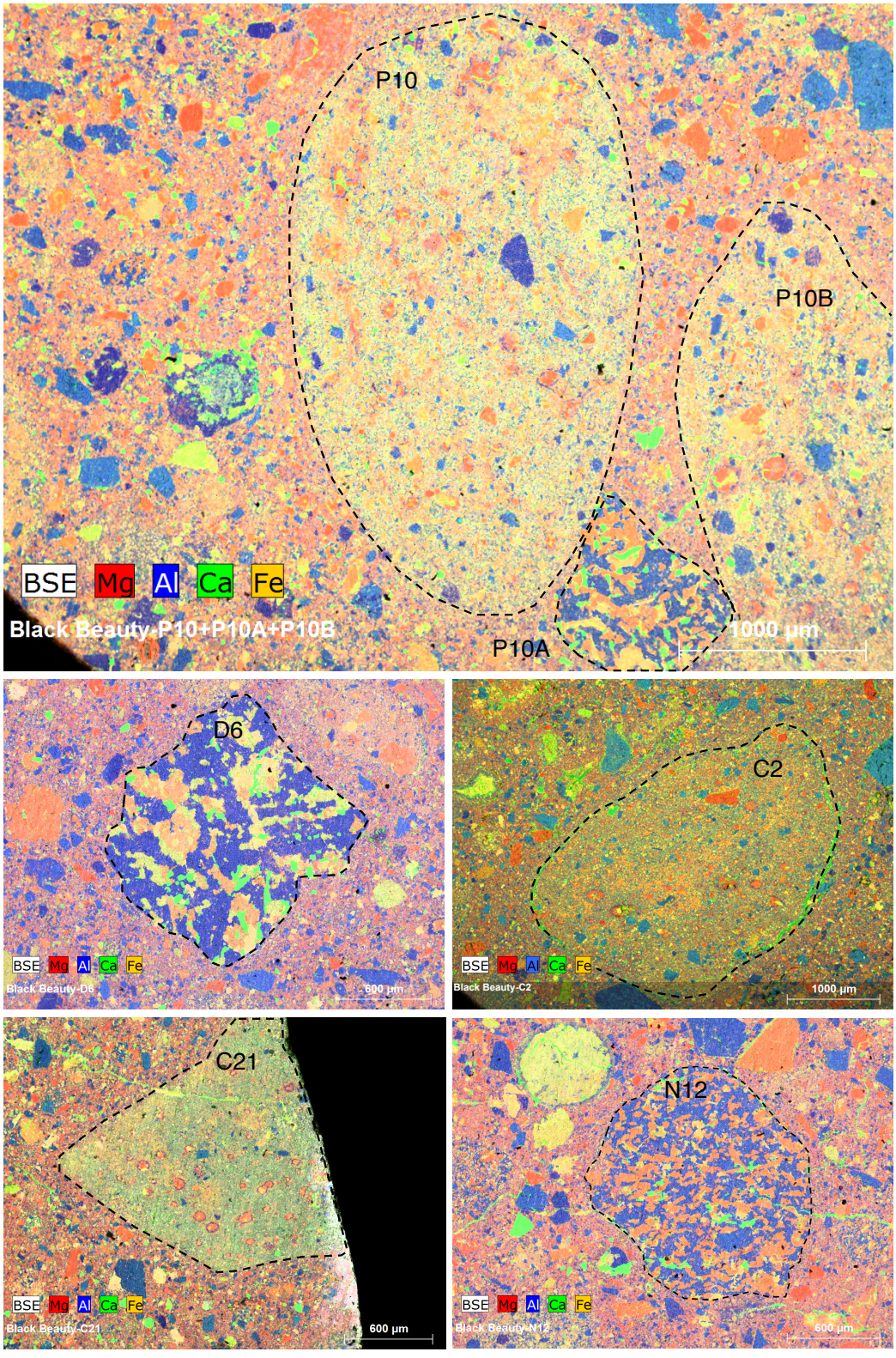

Fig. S14.
Chemical maps for clasts D6, C21, P10, P10A, P10B, C2 and N12.

REFERENCES AND NOTES

1. A. Udry, G. H. Howarth, C. Herd, J. M. D. Day, T. J. Lapen, What martian meteorites reveal about the interior and surface of Mars. *Earth Space Science Open Archive* **55**, 10.1002/essoar.10503123.1 (2020).

2. L. C. Bouvier, M. M. Costa, J. N. Connelly, N. K. Jensen, D. Wielandt, M. Storey, A. A. Nemchin, M. J. Whitehouse, J. F. Snape, J. J. Bellucci, F. Moynier, A. Agranier, B. Gueguen, M. Schönbächler, M. Bizzarro, Evidence for extremely rapid magma ocean crystallization and crust formation on Mars. *Nature* **558**, 586–589 (2018).

3. M. Humayun, A. Nemchin, B. Zanda, R. H. Hewins, M. Grange, A. Kennedy, J.-P. Lorand, C. Göpel, C. Fieni, S. Pont, D. Deldicque, Origin and age of the earliest Martian crust from meteorite NWA 7533. *Nature* **503**, 513–516 (2013).

4. C. B. Agee, N. V. Wilson, F. M. McCubbin, K. Ziegler, V. J. Polyak, Z. D. Sharp, Y. Asmerom, M. H. Nunn, R. Shaheen, M. H. Thiemens, A. Steele, M. L. Fogel, R. Bowden, M. Glamoclija, Z. Zhang, S. M. Elardo, Unique meteorite from early Amazonian Mars: Water-rich basaltic breccia Northwest Africa 7034. *Science* **339**, 780–785 (2013).

5. I. S. E. Carmichael, The redox states of basic and silicic magmas: A reflection of their source regions? *Contrib. Mineral. Petrol.* **106**, 129–141 (1991).

6. K. Righter, S. R. Sutton, L. Danielson, K. Pando, M. Newville, Redox variations in the inner solar system with new constraints from vanadium XANES in spinels. *Am. Mineral.* **101**, 1928–1942 (2016).

7. C. D. K. Herd, J. J. Papike, A. J. Brearley, Oxygen fugacity of martian basalts from electron microprobe oxygen and TEM-EELS analyses of Fe-Ti oxides. *Am. Mineral.* **86**, 1015–1024 (2001).

8. A. R. Santos, C. B. Agee, F. M. McCubbin, C. K. Shearer, P. V. Burger, R. Tartèse, M. Anand, Petrology of igneous clasts in Northwest Africa 7034: Implications for the petrologic diversity of the martian crust. *Geochim. Cosmochim. Acta* **157**, 56–85 (2015).

9. J. Tuff, J. Wade, B. J. Wood, Volcanism on Mars controlled by early oxidation of the upper mantle. *Nature* **498**, 342–345 (2013).

10. M.-A. Millet, N. Dauphas, N. D. Greber, K. W. Burton, C. W. Dale, B. Debret, C. G. Macpherson, G. M. Nowell, H. M. Williams, Titanium stable isotope investigation of magmatic processes on the Earth and Moon. *Earth Planet. Sci. Lett.* **449**, 197–205 (2016).

11. Z. Deng, M. Chaussidon, P. Savage, F. Robert, R. Pik, F. Moynier, Titanium isotopes as a tracer for the plume or island arc affinity of felsic rocks. *Proc. Natl. Acad. Sci. U.S.A.* **116**, 1132–1135 (2019).

12. F. Farges, G. E. Brown Jr., Coordination chemistry of titanium (IV) in silicate glasses and melts: IV. XANES studies of synthetic and natural volcanic glasses and tektites at ambient temperature and pressure. *Geochim. Cosmochim. Acta* **61**, 1863–1870 (1997).

13. A. C. Johnson, S. M. Aarons, N. Dauphas, N. X. Nie, H. Zeng, R. T. Helz, S. J. Romaniello, A. D. Anbar, Titanium isotopic fractionation in Kilauea Iki lava lake driven by oxide crystallization. *Geochim. Cosmochim. Acta* **264**, 180–190 (2019).

14. L. Hoare, M. Klaver, N. S. Saji, J. Gillies, I. J. Parkinson, C. J. Lissenberg, M.-A. Millet, Melt chemistry and redox conditions control titanium isotope fractionation during magmatic differentiation. *Geochim. Cosmochim. Acta* **282**, 38–54 (2020).

15. X. Zhao, S. Tang, J. Li, H. Wang, R. Helz, B. Marsh, X. Zhu, H. Zhang, Titanium isotopic fractionation during magmatic differentiation. *Contrib. Mineral. Petrol.* **175**, 67 (2020).

16. Supplementary text in the Supplementary Materials file.

17. R. Arató, A. Audétat, FeTiMM − A new oxybarometer for mafic to felsic magmas. *Geochem. Perspect. Lett.* **5**, 19–23 (2017).

18. M. J. Toplis, M. R. Carroll, An experimental study of the influence of oxygen fugacity on Fe-Ti oxide stability, phase relations, and mineral—Melt equilibria in ferro-basaltic systems. *J. Petrol.* **36**, 1137–1170 (1995).

19. H. Y. McSween Jr., G. J. Taylor, M. B. Wyatt, Elemental composition of the martian crust. *Science* **324**, 736–739 (2009).

20. W. V. Boynton, G. J. Taylor, L. G. Evans, R. C. Reedy, R. Starr, D. M. Janes, K. E. Kerry, D. M. Drake, K. J. Kim, R. M. S. Williams, M. K. Crombie, J. M. Dohm, V. Baker, A. E. Metzger, S. Karunatillake, J. M. Keller, H. E. Newsom, J. R. Arnold, J. Brückner, P. A. J. Englert, O. Gasnault, A. L. Sprague, I. Mitrofanov, S. W. Squyres, J. I. Trombka, L. d'Uston, H. Wänke, D. K. Hamara, Concentration of H, Si, Cl, K, Fe, and Th in the low- and mid-latitude regions of Mars. *J. Geophys. Res. Planets* **112**, E12S99 (2007).

21. R. Gellert, R. Rieder, J. Brückner, B. C. Clark, G. Dreibus, G. Klingelhöfer, G. Lugmair, D. W. Ming, H. Wänke, A. Yen, J. Zipfel, S. W. Squyres, Alpha particle x-ray spectrometer (APXS): Results from Gusev crater and calibration report. *J. Geophys. Res. Planets* **111**, E02S05 (2006).

22. D. W. Ming, R. Gellert, R. V. Morris, R. E. Arvidson, J. Brückner, B. C. Clark, B. A. Cohen, C. d'Uston, T. Economou, I. Fleischer, G. Klingelhöfer, T. J. McCoy, D. W. Mittlefehldt, M. E. Schmidt, C. Schröder, S. W. Squyres, E. Tréguier, A. S. Yen, J. Zipfel, Geochemical properties of rocks and soils in Gusev Crater, Mars: Results of the alpha particle x-ray spectrometer from Cumberland Ridge to Home Plate. *J. Geophys. Res. Planets* **113**, E12S39 (2008).

23. M. E. Schmidt, J. L. Campbell, R. Gellert, G. M. Perrett, A. H. Treiman, D. L. Blaney, A. Olilla, F. J. Calef III, L. Edgar, B. E. Elliott, J. Grotzinger, J. Hurowitz, P. L. King, M. E. Minitti, V. Sautter, K. Stack, J. A. Berger, J. C. Bridges, B. L. Ehlmann, O. Forni, L. A. Leshin, K. W. Lewis, S. M. McLennan, D. W. Ming, H. Newsom, I. Pradler, S. W. Squyres, E. M. Stolper, L. Thompson, S. VanBommel, R. C. Wiens, Geochemical diversity in first rocks examined by the Curiosity Rover in Gale Crater: Evidence for and significance of an alkali and volatile-rich igneous source. *J. Geophys. Res. Planets* **119**, 64–81 (2014).

24. A. Cousin, V. Sautter, V. Payré, O. Forni, N. Mangold, O. Gasnault, L. Le Deit, J. Johnson, S. Maurice, M. Salvatore, R. C. Wiens, P. Gasda, W. Rapin, Classification of igneous rocks analyzed by ChemCam at Gale crater, Mars. *Icarus* **288**, 265–283 (2017).

25. K. Lodders, A survey of shergottite, nakhlite and chassigny meteorites whole-rock compositions. *Meteorit. Planet. Sci.* **33**, A183–A190 (1998).

26. J. Filiberto, Geochemistry of Martian basalts with constraints on magma genesis. *Chem. Geol.* **466**, 1–14 (2017).

27. A. Udry, N. G. Lunning, H. Y. McSween Jr., R. J. Bodnar, Petrogenesis of a vitrophyre in the martian meteorite breccia NWA 7034. *Geochim. Cosmochim. Acta* **141**, 281–293 (2014).

28. S. Goderis, A. D. Brandon, B. Mayer, M. Humayun, Ancient impactor components preserved and reworked in martian regolith breccia Northwest Africa 7034. *Geochim. Cosmochim. Acta* **191**, 203–215 (2016).

29. R. H. Hewins, B. Zanda, M. Humayun, A. Nemchin, J.-P. Lorand, S. Pont, D. Deldicque, J. J. Bellucci, P. Beck, H. Leroux, M. Marinova, L. Remusat, C. Göpel, E. Lewin, M. Grange, A. Kennedy, M. J. Whitehouse, Regolith breccia Northwest Africa 7533: Mineralogy and petrology with implications for early Mars. *Meteorit. Planet. Sci.* **52**, 89–124 (2017).

30. F. M. McCubbin, J. W. Boyce, T. Novák-Szabó, A. R. Santos, R. Tartèse, N. Muttik, G. Domokos, J. Vazquez, L. P. Keller, D. E. Moser, D. J. Jerolmack, C. K. Shearer, A. Steele, S. M. Elardo, Z. Rahman, M. Anand, T. Delhaye, C. B. Agee, Geologic history of Martian regolith breccia Northwest Africa 7034: Evidence for hydrothermal activity and lithologic diversity in the Martian crust. *J. Geophys. Res. Planets* **121**, 2120–2149 (2016).

31. R. M. G. Armytage, V. Debaille, A. D. Brandon, C. B. Agee, A complex history of silicate differentiation of Mars from Nd and Hf isotopes in crustal breccia NWA 7034. *Earth Planet. Sci. Lett.* **502**, 274–283 (2018).

32. N. K. Jensen, M. M. Costa, J. N. Connelly, M. Bizzarro, Formation of basalt on Mars at ~4443 Ma by impact melting of the primordial crust. *Goldschmidt 2020 abstr.* 1361 (2020); http://goldschmidtabstracts.info/2020/1361.pdf

33. S. Hu, Y. Lin, J. Zhang, J. Hao, W. Xing, T. Zhang, W. Yang, H. Changela, Ancient geologic events on Mars revealed by zircons and apatites from the Martian regolith breccia NWA 7034. *Meteorit. Planet. Sci.* **54**, 850–879 (2019).

34. N. D. Greber, N. Dauphas, I. S. Puchtel, B. A. Hofmann, N. T. Arndt, Titanium stable isotopic variations in chondrites, achondrites and lunar rocks. *Geochim. Cosmochim. Acta* **213**, 534–552 (2017).

35. Z. Deng, F. Moynier, P. A. Sossi, M. Chaussidon, Bridging the depleted MORB mantle and the continental crust using titanium isotopes. *Geochem. Perspect. Lett.* **9**, 11–15 (2018).

36. Z. Deng, F. Moynier, K. van Zuilen, P. A. Sossi, E. A. Pringle, M. Chaussidon, Lack of resolvable titanium stable isotopic variations in bulk chondrites. *Geochim. Cosmochim. Acta* **239**, 409–419 (2018).

37. J. M. Brenan, N. R. Bennett, Z. Zajacz, Experimental results on fractionation of the highly siderophile elements (HSE) at variable pressures and temperatures during planetary and magmatic differentiation. *Rev. Mineral. Geochem.* **81**, 1–87, (2016).

38. M. J. Toplis, A. Corgne, An experimental study of element partitioning between magnetite, clinopyroxene and iron-bearing silicate liquids with particular emphasis on vanadium. *Contrib. Mineral. Petrol.* **144**, 22–37 (2002).

39. W. F. McDonough, S.-s. Sun, The composition of the Earth. *Chem. Geol.* **120**, 223–253 (1995).

40. K. Ziegler, Z. D. Sharp, C. B. Agee, The unique NWA 7034 martian meteorite: Evidence for multiple oxygen isotope reservoirs (44th Lunar and Planetary Science Conference, 2013).

41. A. Ali, I. Jabeen, D. Gregory, R. Verish, N. R. Banerjee, New triple oxygen isotope data of bulk and separated fractions from SNC meteorites: Evidence for mantle homogeneity of Mars. *Meteorit. Planet. Sci.* **51**, 981–995 (2016).

42. A. A. Nemchin, M. Humayun, M. J. Whitehouse, R. H. Hewins, J.-P. Lorand, A. Kennedy, M. Grange, B. Zanda, C. Fieni, D. Deldicque, Record of the ancient martian hydrosphere and atmosphere preserved in zircon from a martian meteorite. *Nat. Geosci.* **7**, 638–642 (2014).

43. D. J. Cherniak, X. Y. Zhang, M. Nakamura, E. B. Watson, Oxygen diffusion in monazite. *Earth Planet. Sci. Lett.* **226**, 161–174 (2004).

44. R. N. Clayton, T. K. Mayeda, Oxygen isotope studies of carbonaceous chondrites. *Geochim. Cosmochim. Acta* **63**, 2089–2104 (1999).

45. J. J. Bellucci, M. J. Whitehouse, A. A. Nemchin, J. F. Snape, G. G. Kenny, R. E. Merle, P. A. Bland, G. K. Benedix, Tracing martian surface interactions with the triple O isotope compositions of meteoritic phosphates. *Earth Planet. Sci. Lett.* **531**, 115977 (2020).

46. P. Lognonné, W. B. Banerdt, W. T. Pike, D. Giardini, U. Christensen, R. F. Garcia, T. Kawamura, S. Kedar, B. Knapmeyer-Endrun, L. Margerin, F. Nimmo, M. Panning, B. Tauzin, J.-R. Scholz, D. Antonangeli, S. Barkaoui, E. Beucler, F. Bissig, N. Brinkman, M. Calvet, S. Ceylan, C. Charalambous, P. Davis, M. van Driel, M. Drilleau, L. Fayon, R. Joshi, B. Kenda, A. Khan, M. Knapmeyer, V. Lekic, J. McClean, D. Mimoun, N. Murdoch, L. Pan, C. Perrin, B. Pinot, L. Pou, S. Menina, S. Rodriguez, C. Schmelzbach, N. Schmerr, D. Sollberger, A. Spiga, S. Stähler, A. Stott, E. Stutzmann, S. Tharimena, R. Widmer-Schnidrig, F. Andersson, V. Ansan, C. Beghein, M. Böse, E. Bozdag, J. Clinton, I. Daubar, P. Delage, N. Fuji, M. Golombek, M. Grott, A. Horleston, K. Hurst, J. Irving, A. Jacob, J. Knollenberg, S. Krasner, C. Krause, R. Lorenz, C. Michaut, R. Myhill, T. Nissen-Meyer, J. ten Pierick, A.C. Plesa, C. Quantin-Nataf, J. Robertsson, L. Rochas, M. Schimmel, S. Smrekar, T. Spohn, N. Teanby, J. Tromp, J. Vallade, N. Verdier, C. Vrettos, R. Weber, D. Banfield, E. Barrett, M. Bierwirth, S. Calcutt, N. Compaire, C. L. Johnson, D. Mance, F. Euchner, L. Kerjean, G. Mainsant, A. Mocquet, J. A. Rodriguez Manfredi, G. Pont, P. Laudet, T. Nebut, S. de Raucourt, O. Robert, C. T. Russell, A. Sylvestre-Baron, S. Tillier, T. Warren, M. Wieczorek, C. Yana, P. Zweifel, Constraints on the shallow elastic and anelastic structure of Mars from Insight seismic data. *Nat. Geosci.* **13**, 213–220 (2020).

47. M. Turbet, C. Gillmann, F. Forget, B. Baudin, A. Palumbo, J. Head, O. Karatekin, The environmental effects of very large bolide impacts on early Mars explored with a hierarchy of numerical models. *Icarus* **335**, 113419 (2020).

48. R. M. Haberle, K. Zahnle, N. G. Barlow, K. E. Steakley, Impact degassing of H_2 on early Mars and its effect on the climate system. *Geophys. Res. Lett.* **46**, 13355–13362 (2019).

49. R. D. Wordsworth, The climate of early Mars. *Annu. Rev. Earth Planet. Sci.* **44**, 381–408 (2016).

50. R. M. Ramirez, R. Kopparapu, M. E. Zugger, T. D. Robinson, R. Freedman, J. F. Kasting, Warming early Mars with CO_2 and H_2. *Nat. Geosci.* **7**, 59–63 (2014).

51. R. Y. Wordsworth, Y. Kalugina, S. Lokshtanov, A. Vigasin, B. Ehlmann, J. Head, C. Sanders, H. Wang, Transient reducing greenhouse warming on early Mars. *Geophys. Res. Lett.* **44**, 665–671 (2017).

52. R. M. Ramirez, R. A. Craddock, T. Usui, Climate simulations of early Mars with estimated precipitation, runoff, and erosion rates. *J. Geophys. Res. Planets* **125**, e2019JE006160 (2020).

53. A. Kamada, T. Kuroda, Y. Kasaba, N. Terada, H. Nakagawa, K. Toriumi, A coupled atmosphere–hydrosphere global climate model of early Mars: A 'cool and wet' scenario for the formation of water channels. *Icarus* **338**, 113567 (2020).

54. J. B. Creech, B. Paul, Isospike: Improved double-spike inversion software. *Geostand. Geoanalytical Res.* **39**, 7–15 (2014).

55. D. Rumble III, J. Farquhar, E. D. Young, C. P. Christensen, In situ oxygen isotope analysis with an excimer laser using F_2 and BrF_5 reagents and O_2 gas as analyte. *Geochim. Cosmochim. Acta* **61**, 4229–4234 (1997).

56. J. W. Valley, N. E. Kitchen, M. J. Kohn, C. R. Niendorf, M. J. Spicuzza, UWG-2, a garnet standard for oxygen isotope ratios: Strategies for high precision and accuracy with laser heating. *Geochim. Cosmochim. Acta* **59**, 5223–5231 (1995).

57. G. Mallmann, H. St. C. O'Neill, The effect of oxygen fugacity on the partitioning of Re between crystals and silicate melt during mantle melting. *Geochim. Cosmochim. Acta* **71**, 2837–2857 (2007).

58. M. A. Elburg, V. S. Kamenetsky, J. D. Foden, A. Sobolev, The origin of medium-K ankaramitic arc magmas from Lombok (Sunda arc, Indonesia): Mineral and melt inclusion evidence. *Chem. Geol.* **240**, 260–279 (2007).

59. P. A. Sossi, S. Klemme, H. St. C. O'Neil, J. Berndt, F. Moynier, Evaporation of moderately volatile elements from silicate melts: Experiments and theory. *Geochim. Cosmochim. Acta* **260**, 204–231 (2019).

60. W. Wang, S. Huang, S. Huang, X. Zhao, Z. Wu, Equilibrium inter-mineral titanium isotope fractionation: Implication for high-temperature titanium isotope geochemistry. *Geochim. Cosmochim. Acta* **269**, 540–553 (2020).

61. F. Gaillard, B. Scaillet, M. Pichavant, J.-M. Bény, The effect of water and fO_2 on the ferric−ferrous ratio of silicic melts. *Chem. Geol.* **174**, 255–273 (2001).